

Quantitative Predictions of Photoelectron Spectra in Amorphous Molecular Solids from Multiscale Quasiparticle Embedding

Gianluca Tirimbò,^{1,*} Xander de Vries,² Christ H.L. Weijtens,² Peter A. Bobbert,³ Tobias Neumann,⁴ Reinder Coehoorn,³ and Björn Baumeier^{1,†}

¹*Department of Mathematics and Computer Science and Institute for Complex Molecular Systems, Eindhoven University of Technology, P.O. Box 513, 5600 MB Eindhoven, The Netherlands*

²*Department of Applied Physics, Eindhoven University of Technology, P.O. Box 513, 5600 MB Eindhoven, The Netherlands*

³*Department of Applied Physics and Institute for Complex Molecular Systems, Eindhoven University of Technology, P.O. Box 513, 5600 MB Eindhoven, The Netherlands*

⁴*Nanomatch GmbH, Hermann-von-Helmholtz-Platz 1, 76344 Eggenstein-Leopoldshafen, Germany*

Ultraviolet Photoelectron Spectroscopy is used intensively for measuring the highest occupied molecular orbital (HOMO) energy of organic semiconductors. However, accurate analyses are hampered by the energetic disorder and the complexity of the excitation process. We present a first-principles study of the spectrum of 2-methyl-9,10-bis(naphthalen-2-yl)anthracene (MADN), an archetypal material, using a deposition simulation, Many Body Green's Function Theory, polarizable film-embedding, and multimode electron-vibrational coupling. The agreement with experiment is excellent, suggesting that our approach provides a route for determining the HOMO energy with accuracy better than 0.1 eV.

Amorphous organic semiconductors are intensively applied in opto-electronic devices such as organic light-emitting diodes (OLEDs) [1–4], photovoltaic cells [5–7] and photodetectors [8–10]. The device properties can be tuned by varying the chemical building blocks or the material processing conditions, and by combining different molecular materials in complex blends or layer stacks. A key parameter determining the functioning of a material in a device is the ionization energy, often termed the highest occupied molecular orbital (HOMO) energy, E_{HOMO} . Relative changes of E_{HOMO} on the order of 0.1 eV can already significantly alter the charge transport through host-guest materials or across internal interfaces between layers. However, even when using the perhaps most direct method for measuring E_{HOMO} , Ultraviolet Photoelectron Spectroscopy (UPS), this level of accuracy has so far not been accomplished. Excitation processes in organic semiconductors are complex, because their localized nature gives rise to strong structural reorganization (polaron formation) and electron-vibration coupling, which leads to shifts, broadening and additional features in the UPS spectrum [11–14]. Combined with the energetic disorder resulting from the amorphous structure and the surface-sensitivity of the measurement, this hampers the unambiguous analysis of the spectra. As a result, the method used for deducing E_{HOMO} from the spectra (from the first peak energy or from an effective onset energy?) is a subject of debate [15–17]. This uncertainty hampers the use of UPS studies for the rational design of new devices, and the combined use of high-resolution UPS, inverse UPS and photoluminescence spectra for obtaining accurate exciton binding energies [18].

Qualitative understanding of the spectra is often sought via gas-phase single-molecule calculations based on density-functional theory (DFT). However, the ob-

tained energy levels need to be artificially shifted and broadened due to the well-known underestimation of the single-particle energy gap by DFT [19, 20] and due to the effects of intermolecular interactions [21]. These calculations lack an explicit link to the molecular morphology, cannot resolve surface and bulk contributions to the density of states (DOS), and do not account for the spectral consequences of the molecular excitation process. This lack of predictive power combined with the ambiguity in extracting the DOS from the experimental data is a big obstacle for the development of layer stacks for organic photovoltaics or next-generation OLEDs, for which the functioning and ultimate performance is already sensitive to energy level variations of only 100 meV.

In this Letter we present a first-principles-based multiscale simulation approach that bridges the current gap between experimental UPS and theoretical models by providing a quantitative prediction of the high-energy part of the UPS spectrum from which the ionization potential is derived. It consists of (i) an accurate evaluation of quasiparticle energy levels within the GW approximation, (ii) the inclusion of morphology effects using polarizable $GW/p\text{MM}$ with long-range interactions (i.e., based on a hybrid quantum-mechanics/molecular-mechanics, MM, approach), (iii) the inclusion of surface sensitivity via the electron attenuation length (EAL), Λ , and (iv) a full-quantum treatment of electron-vibration coupling. We focus here on only one type of initial state (frontier orbitals), and simulate the UPS spectrum for perpendicular emission as a weighted sum of individual molecular environment-dependent densities of states:

$$S_{\text{UPS}}(E) = \sum_{j=1}^{N_{\text{mol}}} S_{\text{el-vib}}(E; \varepsilon_j) \exp\left(-\frac{z_0(x, y) - z_j}{\Lambda}\right), \quad (1)$$

with ε_j the frontier orbital energy level of molecule j , z_j the distance of the molecule’s center-of-mass (COM) to the corrugated surface at $z_0(x, y)$ [22], and $S_{\text{el-vib}}(E; \varepsilon_j)$ the energy-dependent spectral shape due to electron-vibration coupling. N_{mol} is the total number of molecules included in the simulations. In view of the large optical absorption depth, we neglect optical matrix element effects.

As prototypical systems, we study the UPS spectrum for thin films of the α and β isomers of 2-methyl-9,10-bis(naphthalen-2-yl)anthracene (MADN), whose chemical structures are shown as insets in Fig. 1. MADN is a morphologically stable amorphous wide-gap semiconductor [23] that is used extensively as an ambipolar host material in OLEDs containing deep blue fluorescent emitter molecules [24–29]. The methyl substituent disrupts the symmetry and stabilizes the material against crystallization. The type of coupling of the anthracene core and the naphthyl substituents (α or β) affects the planarity of the molecules, and thereby the frontier orbital energies and their distribution in a thin film. We regard MADN as particularly suitable for this study because it exhibits a highest-occupied molecular orbital (HOMO) peak that originates from a single non-degenerate state, located predominantly on the anthracene core. We have experimental UPS data with high resolution (low instrumental broadening) available, and indeed find that the peak full width at half maximum (~ 0.4 eV) is significantly smaller than for many other often-used hole transporting and emitting materials in OLEDs. Section S1 of the Supporting Information (SI) provides the technical details of these experiments. It is furthermore advantageous that the HOMO state is well-separated from the deeper levels. The selection of the two isomers enables us to study the effects of morphology differences and the related effects on energy level shifts due to the small molecular dipole moments.

First, realistic thin-film morphologies are obtained using the Metropolis Monte Carlo-based simulated annealing protocol DEPOSIT [30], mimicking the vapor deposition process. The substrate is represented by a fixed dense layer of MADN. Periodic boundary conditions are used in the directions perpendicular to the growth direction with a side length equal to 10 nm. The final morphologies contain 1000 molecules and are about 10 nm thick. Technical details of the procedure are given in Sec. S2 of the SI. For the following analysis, we remove the bottom 2 nm of the film to avoid spurious effects from the artificial substrate. As a next step, we determine the internal contribution to the HOMO energy of all individual molecules, including quasiparticle corrections within the GW approximation of the many-body Green’s Functions theory [31, 32]. Kohn-Sham (KS) single-particle wave functions $|\phi_i^{\text{KS}}\rangle$ and eigenvalues $\varepsilon_i^{\text{KS}}$ from DFT are used to construct the inverse dielectric function ϵ^{-1} within the random-phase approxi-

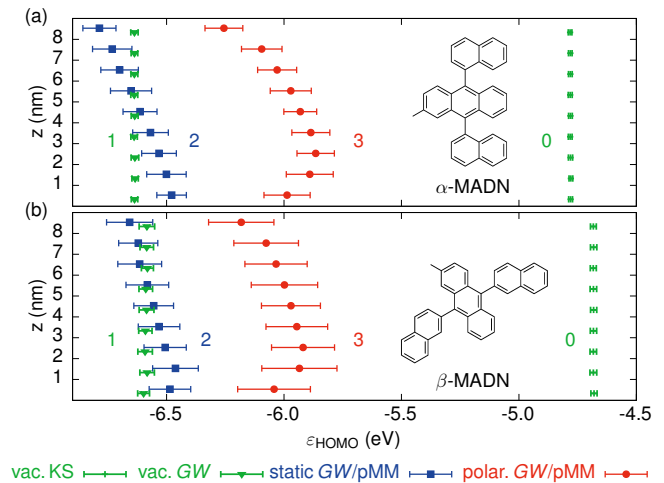


FIG. 1: Layer-averaged energy levels of (a) α -MADN and (b) β -MADN obtained from vacuum KS (0), vacuum GW (1), static (2) and polarizable (3) GW /pMM calculations, respectively. The error bars correspond to the range of \pm one standard deviation.

mation and the electron Green’s function G . This allows us to calculate the screened Coulomb interaction W and the self-energy $\Sigma = iGW$ [33]. The quasiparticle wave functions, expressed as linear combinations of KS states, and their energies ε_i^{GW} are obtained as eigensolutions to the energy-dependent GW Hamiltonian $H_{ij}^{GW}(E) = \varepsilon_i^{\text{KS}} \delta_{ij} + \langle \phi_i^{\text{KS}} | \Sigma(E) - V_{\text{xc}} | \phi_j^{\text{KS}} \rangle$ [34, 35], where V_{xc} is the DFT exchange-correlation potential. In the DFT as well as the GW steps, which are performed using the ORCA [36] and VOTCA-XTP [37] software packages, respectively, we use the PBE functional [38, 39] and the cc-pVTZ basis [40] with its optimized auxiliary basis set [41] for resolution-of-identity techniques (see Sec. S3 of the SI).

Figure 1 shows the laterally-averaged depth dependence of the HOMO energies as resulting from various levels of refinement, labeled “0” to “3”. It shows that GW corrections (“level 1”) to the vacuum KS levels (“level 0”) lower the energies by up to 1.9 eV, nearly uniformly for both isomers. The gas-phase simulations include the molecular deformations in the thin-film morphology, but these cause only a small broadening of the DOS. It is mainly due to disorder in the anthracene-naphthalene torsion angle, which is largest for β -MADN.

Corrections to the intramolecular GW energies due to intermolecular interactions are determined in a coupled quantum-classical (QM/MM) procedure (“quasiparticle embedding”) [42, 43]. Static atomic partial charges from a CHELPG fit to the neutral molecule’s electrostatic potential [44] are used for the classical representation of molecules, and atomic polarizabilities, optimized to reproduce the polarizable volume of the molecule obtained from DFT, account for polarization effects via the induction of atomic dipoles (Thole model [45]). With a cutoff-

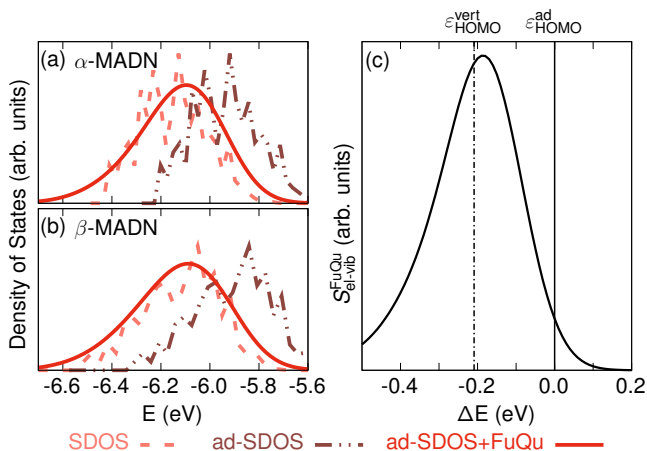


FIG. 2: Frontier orbital surface density-of-states before (SDOS) and after adiabatic correction (ad-SDOS), as well as the simulated UPS spectra within the full-quantum model (ad-SDOS+FuQu) for both α -MADN (a) and β -MADN (b) as obtained from the polarizable $GW/pM\dot{M}$ calculations. Panel (c) shows for β -MADN the shift of single-molecule vertical HOMO level to the adiabatic one at lower binding energies, and the subsequent application of the lineshape function $S_{\text{el-vib}}^{\text{FuQu}}(\Delta E)$ (Eq. 2) which leads to a pronounced broadening (FWHM: 0.25 eV) and shift to higher binding energies with respect to $\varepsilon_{\text{HOMO}}^{\text{ad}}$.

based definition of MM regions in which static and polarizable interactions are taken into account, this model is added directly to the QM Hamiltonian, and coupled solutions are found self-consistently [37]. However, an analysis of the dependence of the obtained excitation energies on the cutoff radius in the thin MADN films reveals slow convergence, implying the need to include long-range electrostatic interactions. We include these by using an Ewald summation method, applied to the Thole model within a subtractive QM/MM scheme, in a manner explained in Sec. S4 of the SI.

When long-range electrostatic interactions are included (static $GW/pM\dot{M}$, level “2”, blue squares in Fig. 1), we find for both isomers a nearly linear z -dependence of the mean HOMO energy, which is symmetric with respect to ε^{GW} . This is due to accumulating net dipole moment contributions parallel to the surface normal during film growth. Even though the dipole moments of the individual molecules are small (0.59 D and 0.56 D for the α and β isomers) and their average net components parallel to the growth axis are only 0.065 D and 0.040 D, respectively, the resulting energy gradients are a few tenths of an eV/nm. Adding polarization effects (polar $GW/pM\dot{M}$, level “3”, red circles in Fig. 1) leads to a shift of the mean of the distributions to lower binding energies. The effect is stronger in the bulk-like center of the film (0.7 eV (0.6 eV) for α -MADN (β -MADN)) than at the vacuum surface (0.5 eV). Differences between the surface and bulk energy level structure of organic mate-

rials are well-known from UPS studies. For crystalline anthracene, e.g., the experimental binding energy difference for the first and second monolayer was found to be 0.3 ± 0.15 eV [46]. A similar effect is seen in Fig. 1 for the first molecular layer near the vacuum surface, which after subtracting the energy gradient due to dipole orientation shows an increase of the binding energy of about 0.15 eV. Since we simulate freestanding thin films, we also note modifications from the bulk-like behavior at the bottom surface with $z = 0$. In view of our interest in analyzing the UPS spectrum after irradiation from the positive z direction, which is only sensitive to the energy level structure in a thin zone near the top vacuum surface, we focus on that region.

To this end the surface density-of-states (SDOS) is obtained by weighting the z -dependent frontier orbital energy with the exponential function from Eq. 1, i.e. $\text{SDOS}(E) = \sum_j \delta(E - \varepsilon_j(z_j)) \exp\left(-\frac{z_0(x,y) - z_j}{\Lambda}\right)$. We adopt a value of $\Lambda = 1$ nm as suggested from experiment. It is compatible with estimates of the inelastic mean free path of the electrons within the Random-Phase Approximation using GW energies (see Sect. S5 of the SI), which we consider an upper limit to the EAL. The SDOS as shown in Fig. 2(a,b) (dashed line) is based on vertical excitation energies and therefore does not include the effect of the intramolecular reorganization process upon charge removal and the associated shift and lineshape broadening via carrier-vibration coupling. Analogous to the full-quantum (FuQu) approach for inter-molecular charge transfer [47], which approximates the potential energy surface of the excited molecule in the independent mode displaced harmonic oscillator model [48], we find that the spectral shape due to coupling of the photoelectrons with vibrational modes k with an energy $\hbar\omega_k$ and a coupling energy λ_k is given by

$$S_{\text{el-vib}}^{\text{FuQu}}(\Delta E) = \frac{1}{2\pi\hbar} \int_{-\infty}^{+\infty} e^{i\frac{\Delta E}{\hbar}t} e^{-G(0)} e^{G(t)} dt, \quad (2)$$

where $G(t) = \sum_k \frac{\lambda_k}{\hbar\omega_k} \left(\coth\left(\frac{\hbar\omega_k}{2k_B T}\right) \cos(\omega_k t) + i \sin(\omega_k t) \right)$. The energy difference ΔE is by derivation relative to an adiabatic excitation energy that can in our model be estimated as $\varepsilon_{\text{HOMO}}^{\text{ad}} = \varepsilon_{\text{HOMO}}^{\text{vert}} + \sum_k \lambda_k$. As shown in Fig. 2(c) for a single β -MADN molecule (α -MADN shows a very similar behavior) this first results in a shift of the reference energy to higher energy before electron-vibration coupling then leads to a shift of the spectral peak to lower energies with respect to $\varepsilon_{\text{HOMO}}^{\text{ad}}$ and to a broadening of 0.25 eV [49]. The same trends are also observed for the adiabatic (ad-)SDOS and the spectral function (ad-SDOS+FuQu, equivalent to $S_{\text{UPS}}(E)$ in Eq. 1) of the films as shown in Fig. 2(a,b) for polar $GW/pM\dot{M}$.

Figure 3 shows the final UPS spectra of the frontier orbital of α - and β -MADN thin films simulated for the four different levels of theory, together with the experimental data. Characteristics of the signals (maximum

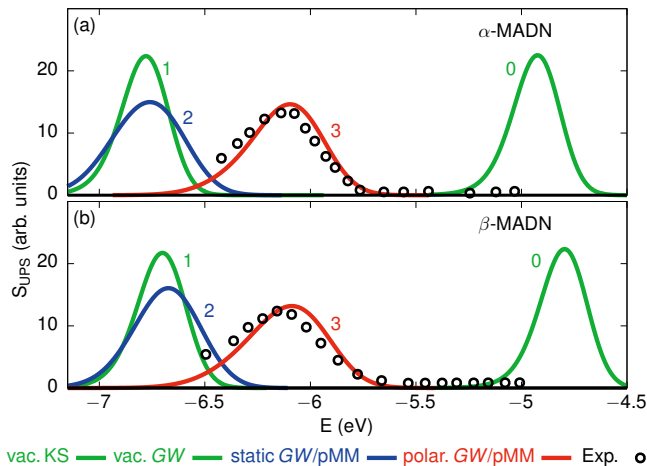


FIG. 3: UPS spectra for α -MADN (a) and β -MADN (b). Curves 0–3 give the UPS as depth weighted DOS with vertical-to-adiabatic shift and vibrational broadening via Eq. 2 predicted from vacuum KS (0), GW (1), static (2) and polarizable GW/pMM (3) calculations, respectively. The closed circles give the experimental spectra, obtained using He-I radiation (21.2 eV). The experimental resolution is $\sigma = 0.05$ eV, and has no significant effect on the final spectral width.

position, onset, and FWHM) are listed in Tab. I. Clearly, the energetic position of the simulated peaks for the different methods reflects the variations discussed for the layer-averages in Fig. 1. Comparison to the reference experimental spectrum now allows assessment of the quality of the various methods and the importance of the individual processes for the analysis of the experiment. Simulations based on vacuum energies which exclude the effects of inhomogeneous local electric fields and environment polarization either over- (KS) or underestimate (GW) the energy of the peak maximum by up to 1.3 eV. The FWHM is nearly exclusively determined by the single-molecule spectral function and results about a third smaller than measured. Inclusion of static local field effects in GW/pMM does not noticeably affect the peak maximum but the additional disorder contributes to further broaden the signal. Accounting for the polarization response of the material upon quasiparticle excitation in GW/pMM we obtain a simulated UPS signal in excellent agreement with the measurement: the largest deviation is found for the peak maximum of β -MADN and amounts to only 50 meV, which is also the experimental resolution. Most importantly, the comparison emphasizes that it is possible to achieve a predictive modeling of frontier orbital energies at the accuracy needed for an accurate understanding and prediction of device performance. The fact that we achieve the same accuracy by studying two isomers, with different molecular structures and thin film morphologies, supports the robustness of our approach. The bulk adiabatic ionization energy, which would be needed in device simula-

TABLE I: Characteristics of the predicted UPS spectrum (see caption of Fig. 3) for α -MADN and β -MADN at different levels of the multiscale quasiparticle embedding procedure. HOMO peak position (Max.), onset, and the full width at half maximum (FWHM) (all in eV) are compared to the respective experimental results.

	vacuum		GW/pMM		Exp.
	KS	GW	Static	Polar	
α-MADN					
Max.	-4.92	-6.78	-6.76	-6.10	-6.12
Onset	-4.71	-6.57	-6.44	-5.79	-5.79
FWHM	0.25	0.25	0.39	0.39	0.37
β-MADN					
Max.	-4.80	-6.70	-6.67	-6.09	-6.14
Onset	-4.58	-6.48	-6.37	-5.75	-5.73
FWHM	0.25	0.26	0.36	0.41	0.42

tions, may be obtained from a linear extrapolation of the bulk polar GW/pMM energies shown in Fig. 1, plus the reorganization energy $\epsilon_{\text{HOMO}}^{\text{ad}} - \epsilon_{\text{HOMO}}^{\text{vert}}$ of 0.21 eV. The resulting values, $-5.91(-5.89) \pm 0.05$ eV for $\alpha(\beta)$ -MADN, are located in between the UPS peak and onset energies (see Tab. I). Using either the peak or the onset value would, in this case, thus introduce an error of about 0.1 eV or more. Our refined protocol for the analysis of UPS measurements provides a methodology for avoiding such an error.

To summarize, we have developed a multiscale approach that provides the material structure, the electronic interactions at a state-of-the-art (Green’s function) level of quantum chemistry embedded in a polarizable molecular mechanics environment, and including the vibrational modes that are excited in the experiment to provide a prediction of the UPS spectrum of frontier orbitals in amorphous molecular solids. Our work shows how the spectrum is related to the vertical and adiabatic ionization potential and its disorder-induced distribution in the bulk of the organic semiconductor, and shows thereby how the results of UPS measurements can be used in predictive analytical theory and numerical device simulations.

ACKNOWLEDGMENTS

This work has been supported by the Innovational Research Incentives Scheme Vidi of the Netherlands Organisation for Scientific Research (NWO) with project number 723.016.002 and by Horizon-2020 EU project MOSTOPHOS (Project No. 646259, XdV)

* Electronic address: g.tirimbo@tue.nl

- † Corresponding author; Electronic address: b.baumeier@tue.nl
- [1] C. W. Tang and S. A. VanSlyke, *Appl Phys Lett* **51**, 913 (1987).
 - [2] J. Kido, M. Kimura, and K. Nagai, *Science* **267**, 1332 (1995).
 - [3] M. A. Baldo, D. F. O'Brien, Y. You, A. Shoustikov, S. Sibley, M. E. Thompson, and S. R. Forrest, *Nature* **395**, 151 (1998).
 - [4] C. Adachi, *Jpn. J Appl Phys* **53**, 060101 (2014).
 - [5] J. J. M. Halls, C. A. Walsh, N. C. Greenham, E. A. Marseglia, R. H. Friend, S. C. Moratti, and A. B. Holmes, *Nature* **376**, 498 (1995).
 - [6] G. Yu, J. Gao, J. C. Hummelen, F. Wudl, and A. J. Heeger, *Science* **270**, 1789 (1995).
 - [7] W. Zhao, S. Li, H. Yao, S. Zhang, Y. Zhang, B. Yang, and J. Hou, *J Amer Chem Soc* **139**, 7148 (2017).
 - [8] P. Peumans, A. Yakimov, and S. R. Forrest, *J Appl Phys* **93**, 3693 (2003).
 - [9] R. D. Jansen-van Vuuren, A. Armin, A. K. Pandey, P. L. Burn, and P. Meredith, *Adv Mater* **28**, 4766 (2016).
 - [10] M. Kielar, O. Dhez, G. Pecastaings, A. Curutchet, and L. Hirsch, *Sci. Repts* **6**, 39201 (2016).
 - [11] W. R. Salaneck, C. B. Duke, W. Eberhardt, E. W. Plummer, and H. J. Freund, *Phys Rev Lett* **45**, 280 (1980).
 - [12] M. Malagoli, V. Coropceanu, D. A. da Silva Filho, and J. L. Brédas, *J Chem Phys* **120**, 7490 (2004).
 - [13] S. Kera, H. Yamane, and N. Ueno, *Prog. Surf. Sci.* **84**, 135 (2009).
 - [14] S. Kera and N. Ueno, *J. Electron Spectrosc. Relat. Phenom.* **204**, 2 (2015).
 - [15] I. G. Hill, A. Kahn, Z. G. Soos, and R. A. Pascal, *Chem Phys Lett* **327**, 181 (2000).
 - [16] B. W. D'Andrade, S. Datta, S. R. Forrest, P. Djurovich, E. Polikarpov, and M. E. Thompson, *Org. Electron.* **6**, 11 (2005).
 - [17] S. Krause, M. B. Casu, A. Schöll, and E. Umbach, *New J Phys* **10**, 085001 (2008).
 - [18] H. Yoshida, K. Yamada, J. Tsutsumi, and N. Sato, *Phys Rev B* **92**, 075145 (2015).
 - [19] J. P. Perdew, *Int J Quantum Chem* **28**, 497 (1985).
 - [20] P. Mori-Sánchez, A. J. Cohen, and W. Yang, *Phys Rev Lett* **100**, 146401 (2008).
 - [21] S. M. Tadayyon, H. M. Grandin, K. Griffiths, L. L. Coatsworth, P. R. Norton, H. Aziz, and Z. D. Popovic, *Org. Electron.* **5**, 199 (2004).
 - [22] The surface profile $z_0(x, y)$ is determined from a fit to the highest COM coordinates. For surface corrugations $\delta z \ll \lambda_{in}$, $\exp[-(z_0(x, y) - z_j)/\lambda_{in}] \simeq \exp[-(z_0 - z_j)/\lambda_{in}]$ in Eq. 1.
 - [23] M.-T. Lee, H.-H. Chen, C.-H. Liao, C.-H. Tsai, and C. H. Chen, *Appl Phys Lett* **85**, 3301 (2004).
 - [24] M.-T. Lee, C.-H. Liao, C.-H. Tsai, and C.-H. Chen, *Adv Mater* **17**, 2493 (2005).
 - [25] C.-H. Liao, M.-T. Lee, C.-H. Tsai, and C. H. Chen, *Appl Phys Lett* **86**, 203507 (2005).
 - [26] M.-H. Ho, Y.-S. Wu, S.-W. Wen, M.-T. Lee, T.-M. Chen, C. H. Chen, K.-C. Kwok, S.-K. So, K.-T. Yeung, Y.-K. Cheng, et al., *Appl Phys Lett* **89**, 252903 (2006).
 - [27] J. Huang, J.-H. Su, and H. Tian, *J Mater Chem* **22**, 10977 (2012).
 - [28] M.-H. Ho, M.-Y. Liu, K.-H. Lin, C. H. Chen, and C. W. Tang, *SID Symp. Dig. Tech. Pap.* **41**, 552 (2010).
 - [29] D. H. Ahn, J. H. Jeong, J. Song, J. Y. Lee, and J. H. Kwon, *ACS Appl Mater Interf* **10**, 10246 (2018).
 - [30] T. Neumann, D. Danilov, C. Lennartz, and W. Wenzel, *J Comput Chem* **34**, 2716 (2013).
 - [31] L. J. Sham and T. M. Rice, *Phys Rev* **144**, 708 (1966).
 - [32] L. Hedin and S. Lundqvist, in *Solid State Physics*, edited by F. Seitz, D. Turnbull, and H. Ehrenreich (Academic Press, 1970), vol. 23, pp. 1–181.
 - [33] G. Onida, L. Reining, and A. Rubio, *Rev Mod Phys* **74**, 601 (2002).
 - [34] W. G. Aulbur, L. Jönsson, and J. W. Wilkins, in *Solid State Physics*, edited by H. Ehrenreich and F. Spaepen (Academic Press, 2000), vol. 54, pp. 1–218.
 - [35] M. Rohlfing, *Int J Quantum Chem* **80**, 807 (2000).
 - [36] F. Neese, *Wiley Interdiscip. Rev. Comput. Mol. Sci.* **2**, 73 (2012).
 - [37] J. Wehner, L. Brombacher, J. Brown, C. Junghans, O. Çaylak, Y. Khalak, P. Madhikar, G. Tirimbò, and B. Baumeier, *J Chem Theory Comput* **14**, 6253 (2018).
 - [38] J. P. Perdew, K. Burke, and M. Ernzerhof, *Phys Rev Lett* **77**, 3865 (1996).
 - [39] Comparative calculations with the hybrid PBEH [50] functional show no significant starting-point dependence of the ε_i^{GW} .
 - [40] R. A. Kendall, T. H. Dunning, and R. J. Harrison, *J Chem Phys* **96**, 6796 (1992).
 - [41] F. Weigend, A. Köhn, and C. Hättig, *J. Chem. Phys.* **116**, 3175 (2002).
 - [42] F. May, B. Baumeier, C. Lennartz, and D. Andrienko, *Phys Rev Lett* **109**, 136401 (2012).
 - [43] T. Schwabe, K. Sneskov, J. M. Haugaard Olsen, J. Kongsted, O. Christiansen, and C. Hättig, *J Chem Theory Comput* **8**, 3274 (2012).
 - [44] C. M. Breneman and K. B. Wiberg, *J Comput Chem* **11**, 361 (1990).
 - [45] A. Stone, *The Theory of Intermolecular Forces, 2nd Edition* (Oxford University Press, Oxford, 2013), 2nd ed., ISBN 978-0-19-967239-4.
 - [46] W. R. Salaneck, *Phys Rev Lett* **40**, 60 (1978).
 - [47] X. de Vries, P. Friederich, W. Wenzel, R. Coehoorn, and P. A. Bobbert, *Phys. Rev. B* **97**, 075203 (2018).
 - [48] T. Petrenko and F. Neese, *J. Chem. Phys.* **127**, 164319 (2007).
 - [49] The absence of satellite peaks in Fig. 2(c), as usually seen for gas-phase spectra of, e.g. pentacene, is due to coupling of multiple modes in α - and β -MADN, which smears out the structures.
 - [50] M. Ernzerhof and G. E. Scuseria, *J Chem Phys* **110**, 5029 (1999).

Quantitative Predictions of Photoelectron Spectra in Amorphous Molecular Solids from Multiscale Quasiparticle Embedding

Gianluca Tirimbò,^{1,*} Xander de Vries,² Christ H.L. Weijtens,² Peter A. Bobbert,³ Tobias Neumann,⁴ Reinder Coehoorn,³ and Björn Baumeier^{1,†}

¹*Department of Mathematics and Computer Science and Institute for Complex Molecular Systems, Eindhoven University of Technology, P.O. Box 513, 5600 MB Eindhoven, The Netherlands*

²*Department of Applied Physics, Eindhoven University of Technology, P.O. Box 513, 5600 MB Eindhoven, The Netherlands*

³*Department of Applied Physics and Institute for Complex Molecular Systems, Eindhoven University of Technology, P.O. Box 513, 5600 MB Eindhoven, The Netherlands*

⁴*Nanomatch GmbH, Hermann-von-Helmholtz-Platz 1, 76344 Eggenstein-Leopoldshafen, Germany*

S1. EXPERIMENTAL DETAILS

Experiments were done in a multi-chamber VG EscaLab II system with a base pressure of the deposition and the analyzer chamber in the upper 10^{-6} and the lower 10^{-8} Pa range respectively. α - and β -MADN (Lumtec) were deposited by high-vacuum ($8 \cdot 10^{-6}$ Pa) thermal evaporation onto in situ sputter-cleaned Au-coated Si-substrates at a rate of about 1 nm/min. The deposited films were transferred under ultra high vacuum (UHV) between the deposition and the analyzer chamber. UPS spectra were recorded at -6 V bias using HeI radiation generated in a differentially-pumped discharge lamp.

S2. MORPHOLOGY SIMULATION

Digital twins of thin films with atomistic resolution were generated for both materials using Nanomatch software modules Deposit, Parametrizer and Dihedral Parametrizer. Deposit is a Metropolis Monte-Carlo based single molecule deposition protocol mimicking physical vapor deposition (PVD)¹ and provides molecular morphologies that exhibit commonly observed PVD characteristic features.^{2,3} Each molecule was deposited using 32 simulated annealing cycles with 120000 Monte-Carlo steps each, annealing from 4000 K to 300 K. Periodic boundary conditions were applied in the directions perpendicular to the growth direction. The energy at each simulation step was computed using customized force-fields generated using the Parametrizer module. These force-fields comprise Coulomb electrostatics based on partial charges obtained from an electrostatic potential fit,⁴ Lennard-Jones potentials to account for Van-der-Waals interaction and Pauli repulsion, and compound specific dihedral force-fields with quantum chemistry accuracy generated by the Dihedral Parametrizer.

S3. COMPUTATIONAL DETAILS OF THE GW CALCULATIONS

We summarize the major concepts behind the *GW* approximation and its implementation in VOTCA-XTP.⁵ We restrict the discussion to a closed shell system of N electrons with spin singlet ground state, whose properties can be calculated using Density-Functional Theory (DFT) by solving the *Kohn-Sham* (KS) equations⁶

$$[T_0 + V_{\text{ext}} + V_{\text{Hartree}} + V_{\text{xc}}]|\phi_i^{\text{KS}}\rangle = \epsilon_i^{\text{KS}}|\phi_i^{\text{KS}}\rangle \quad (1)$$

in which T_0 is the kinetic energy operator, V_{ext} an external potential, V_{Hartree} the Hartree potential, and V_{xc} the exchange-correlation potential. In Table S1 we show a comparison of calculated gas-phase energy levels (in eV) for α -MADN and β -MADN obtained using different xc-functionals with the cc-pVTZ basis. Note the variation in the results, e.g., in the HOMO energy of α -MADN: -4.79 eV (PBE) and -5.55 eV (PBEH). It is a consequence of the spurious self-interaction in the functionals and the inadequacy of DFT to describe electronically excited states. Instead, particle-like excitations, known as quasiparticles (QP), in which an electron is added to or removed from the N electron system ground state, are described by the one-body Green's function, G_1 .^{7,8} This function obeys a Dyson-type equation of motion, which in spectral representation is:

$$[H_0 + \Sigma(E)]G_1(E) = EG_1(E), \quad (2)$$

where $H_0 = T_0 + V_{\text{ext}} + V_{\text{Hartree}}$, is the DFT Hamiltonian, while the exchange-correlation effects are described by the electron self-energy operator $\Sigma(E)$. It can be shown that Eq. 2 is part of a closed set of coupled equations, known as

TABLE S1: Comparison of calculated gas-phase energy levels (in eV) for α -MADN and β -MADN obtained using the PBE and PBEH functionals with the cc-pVTZ basis set, within KS-DFT (KS), including perturbative quasiparticle corrections (PQP), and after diagonalization of the quasiparticle Hamiltonian (DQP), respectively.

α -MADN				β -MADN			
	KS (eV)	PQP (eV)	DQP (eV)		KS (eV)	PQP (eV)	DQP (eV)
PBE				PBE			
HOMO-2	-5.412	-7.538	-7.597	HOMO-2	-5.459	-7.616	-7.690
HOMO-1	-5.396	-7.524	-7.595	HOMO-1	-5.456	-7.614	-7.682
HOMO	-4.786	-6.610	-6.689	HOMO	-4.762	-6.574	-6.650
LUMO	-2.468	-0.245	-0.348	LUMO	-2.457	-0.231	-0.335
LUMO+1	-2.011	0.536	0.424	LUMO+1	-2.030	0.514	0.384
LUMO+2	-2.000	0.550	0.435	LUMO+2	-2.027	0.520	0.414
PBEH				PBEH			
HOMO-2	-6.270	-7.570	-7.611	HOMO-2	-6.324	-7.652	-7.701
HOMO-1	-6.256	-7.559	-7.606	HOMO-1	-6.321	-7.652	-7.693
HOMO	-5.548	-6.645	-6.702	HOMO	-5.521	-6.615	-6.670
LUMO	-1.755	-0.218	-0.313	LUMO	-1.744	-0.204	-0.297
LUMO+1	-1.200	0.544	0.444	LUMO+1	-1.230	0.514	0.411
LUMO+2	-1.189	0.561	0.457	LUMO+2	-1.219	0.533	0.438

Hedin equations.^{9,10} KS-DFT is an approximated solution for the excited electrons problem, in which $\Sigma \sim V_{xc}$, whose associated Green's function G_0 , solution of Eq. 2, is $G_0(E) = \sum_i \frac{|\phi_i^{KS}\rangle\langle\phi_i^{KS}|}{E - \epsilon_i^{KS} \pm i\eta}$.

A beyond-DFT solution of this system is given by the *GW approximation*, in which

$$\Sigma = iG_1W, \quad (3)$$

where $W = \epsilon^{-1}v_c$ is the screened Coulomb interaction and $v_c(\mathbf{r}, \mathbf{r}') = 1/|\mathbf{r} - \mathbf{r}'|$ is the bare Coulomb interaction, respectively. The inverse dielectric function, ϵ^{-1} , is calculated in the *random-phase approximation* (RPA).¹¹ Within this *GW* approximation, Eq. 2 is transformed into a Dyson equation of motion for the quasiparticles:^{12,13}

$$\left[H_0 + \Sigma(\epsilon_i^{\text{QP}}) \right] |\phi_i^{\text{QP}}\rangle = \epsilon_i^{\text{QP}} |\phi_i^{\text{QP}}\rangle, \quad (4)$$

where ϵ_i^{QP} are the one particle excitation energies of the system (i.e., the QP electron and holes states) and $|\phi_i^{\text{QP}}\rangle$ the quasiparticle wave functions.

In practice, these quasiparticle wave functions are expanded in terms of the KS states according to $|\phi_i^{\text{QP}}\rangle = \sum_j a_j^i |\phi_j^{\text{KS}}\rangle$. Assuming that $|\phi_i^{\text{QP}}\rangle \approx |\phi_i^{\text{KS}}\rangle$, the quasiparticle energies can be obtained perturbatively (we refer to this stage as PQP) as

$$\epsilon_i^{\text{QP}} = \epsilon_i^{\text{KS}} + \Delta\epsilon_i^{\text{GW}} = \epsilon_i^{\text{KS}} + \langle\phi_i^{\text{KS}}|\Sigma(\epsilon_i^{\text{QP}}) - V_{xc}|\phi_i^{\text{KS}}\rangle. \quad (5)$$

The determination of ϵ_i^{QP} via Eq. 5 typically holds if the off-diagonal elements of the self-energy, i.e., $\langle\phi_j^{\text{KS}}|\Sigma(E)|\phi_i^{\text{KS}}\rangle$, are small. Otherwise, expressing the QP wave functions as a linear combination of KS states need to be fully taken into account. Quasiparticle wave functions and energies can then be obtained by diagonalizing the energy dependent QP Hamiltonian (we refer to this stage as DQP)

$$H_{i,j}^{\text{QP}}(E) = \epsilon_i^{\text{KS}}\delta_{i,j} + \langle\phi_i^{\text{KS}}|\Sigma(E) - V_{xc}|\phi_j^{\text{KS}}\rangle. \quad (6)$$

Both the correction term $\Delta\epsilon_i^{\text{GW}}$ and the non-local, energy-dependent microscopic dielectric function calculated within the RPA depend on ϵ_i^{QP} .^{11,14} Solutions to Eq. 5 therefore in general need to be found self-consistently. With this procedure, called *evGW* in literature, the quasiparticle energies are additionally updated in the RPA calculation until eigenvalues (ev) self-consistency. Some technical information about the implementation used in this work: we use 10^{-5} Hartree as convergence limit for self-consistent cycles, the number of levels taken in account for the QP calculations, i.e number of occupied and unoccupied levels, is 327, while for the RPA step the level range is 1385.

VOTCA-XTP employs a generalized plasmon pole model (PPM) as outlined in Ref. 14 to perform the frequency integration. This model allows for a quick evaluation of the self-energy, but at the same time turns the self-energy

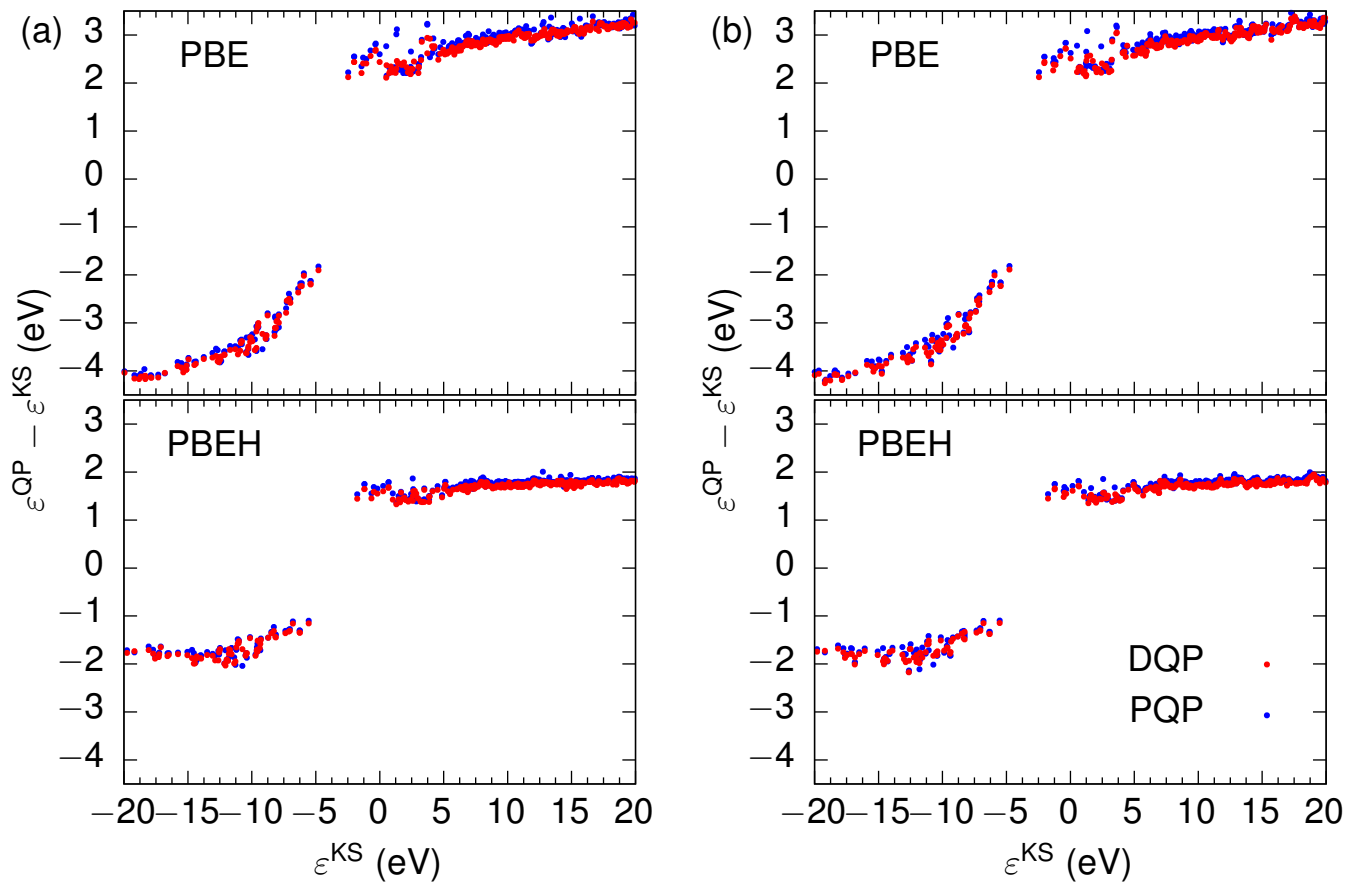


FIG. S1: Calculated quasiparticle corrections as a function of Kohn-Sham energy for α -MADN (left column) and β -MADN (right column) based on different DFT functionals.

into a real operator. VOTCA-XTP can read this information from standard packages using Gaussian-type orbitals (GTOs) as basis functions $\{\psi_i(\mathbf{r})\}$ to express

$$\phi_i^{\text{KS}}(\mathbf{r}) = \sum_{j=0}^M X_{ij} \psi_j(\mathbf{r}). \quad (7)$$

Matrix elements $\langle \phi_i^{\text{KS}} | V_{\text{xc}} | \phi_j^{\text{KS}} \rangle$ needed in Eq. 5 are numerically integrated using spherical Lebedev and radial Euler-Maclaurin grids as used in NWChem,¹⁵ with XC functionals provided by the *LibXC* library.¹⁶ For all this work calculations we used the cc-pVTZ basis set.¹⁷

In the evaluation of the self-energy, four-center Coulombic integrals of the form

$$(ij|kl) = \iint d\mathbf{r} d\mathbf{r}' \psi_i(\mathbf{r}) \psi_j(\mathbf{r}) v_c(\mathbf{r}, \mathbf{r}') \psi_k(\mathbf{r}') \psi_l(\mathbf{r}') \quad (8)$$

need to be calculated. VOTCA-XTP makes use of the resolution-of-identity approximation (namely the RI-V approximation) reduce the scaling from N^4 to N^3 , with N is the number of basis function. An auxiliary basis set $\{\chi_\nu(\mathbf{r})\}$ is introduced so that Eq. 8 are rewritten in the form

$$(ij|kl) \approx \sum_{\nu, \mu} (ij|\nu) (\nu|\mu)^{-1} (\mu|kl). \quad (9)$$

Here $(\nu|\mu)^{-1}$ is the inverse of the two-center coulomb matrix $(\nu|\mu) = \iint d\mathbf{r}_1 d\mathbf{r}_2 \chi_\nu(\mathbf{r}_1) v_c(\mathbf{r}_1, \mathbf{r}_2) \chi_\mu(\mathbf{r}_2)$ and $(ij|\nu) = \iint d\mathbf{r}_1 d\mathbf{r}_2 \psi_i(\mathbf{r}_1) \psi_j(\mathbf{r}_2) v_c(\mathbf{r}_1, \mathbf{r}_2) \chi_\nu(\mathbf{r}_2)$ is the three-center Coulomb matrix. Specifically, we used the auxiliary RI-basis for the cc-pVTZ basis from Ref. 18.

Figure S1 illustrates the effects of different functionals used in the underlying DFT ground state calculation on the computed quasiparticle levels (both in the PQP and DQP variant). The correction to the KS-levels is not constant

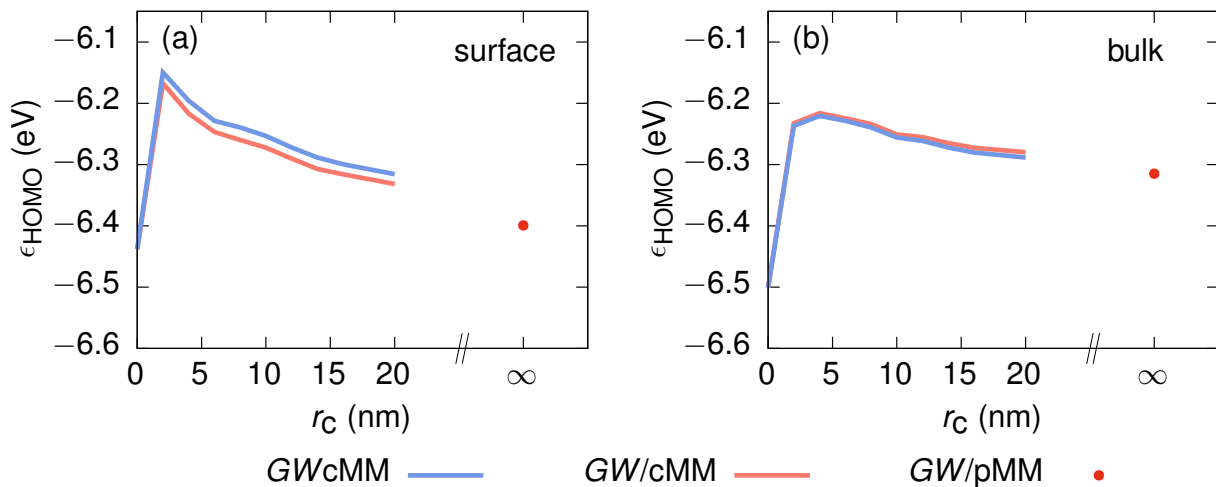


FIG. S2: Comparison of different molecular mechanics embedding setups for the quasiparticle calculations including long-range electrostatic effects for (a) a surface and (b) a bulk molecule in the β -MADN thin film. For the cutoff-based GWcMM (blue line) and GW/cMM (red line) methods, the cutoff length r_c is varied showing only a slow convergence of the calculated ϵ_{HOMO} . The value at $r_c = \infty$ indicates the result after periodic embedding (GW/pMM). In all variants, only the quasiparticle state is considered polarizable while the molecules in the MM region are described by static point charges.

and varies between occupied and unoccupied states. We can see that for the PBE functional the QP correction is more pronounced than in the case of the PBEH hybrid functional, which already contains part of the exchange contributions to the self-energy operator. Despite the different energy-dependent corrections, the final quasiparticle energies as listed in Tab. S1 do not show a noticeable dependence on the DFT starting point. The final DQP quasiparticle HOMO energy varies only by 0.01 eV (0.02 eV) for α -MADN (β -MADN) among the two functionals.

S4. MOLECULAR MECHANICS EMBEDDING OF QUASIPARTICLE CALCULATIONS

In this work we embed the quantum (QM) quasiparticle calculations on GW level into a classical environment described by molecular mechanics (MM) models. In general, the MM part is represented by static atomic multipole moments Q_t^a ¹⁹ where t indicates the multipole rank and a the associated atom in the molecule. Furthermore on each atomic site a polarizability $\alpha_{tt'}^{aa'}$ is assigned, leading to the induced moments ΔQ_t^a due to the field generated by moment t' of atom a' :

$$\Delta Q_t^a = - \sum_B \alpha_{tt'(s)}^{aa'} T_{t'u}^{a'b} (Q_u^b + \Delta Q_u^b). \quad (10)$$

The classical total energy of a system in the state (s) (i.e neutral ($s = n$) or charged ($s = \text{qp}$, via quasiparticle excitation)) composed of A molecules is given by¹⁹

$$E_{\text{MM}}^{(s)} = \frac{1}{2} \sum_{A,A'} (Q_t^{a(s)} + \Delta Q_t^{a(s)}) T_{tu}^{aa'} Q_u^{a'(s)}, \quad (11)$$

where interactions between the multipole moments Q_t^a and $Q_u^{a'}$ are described by the interaction tensor $T_{tu}^{aa'}$. We use a repeated-index summation convention for the multipole and site indices, respectively.

A. Comparison of cutoff-based and periodic embedding schemes

When combining QM and MM methods, various scenarios for the coupling are possible. First, the MM environment, defined by a cutoff distance r_c around the QM molecule, is explicitly included in the GW calculation as an additional external potential. In this GWcMM scheme, the QM region is directly polarized by the multipole distribution (and vice versa). This scheme is also referred to as *additive scheme* in the literature.²⁰ To assess the effects of the choice of cutoff, we show in Fig. S2 (blue curve) the calculated ϵ_{HOMO} as a function of r_c for a molecule at the surface

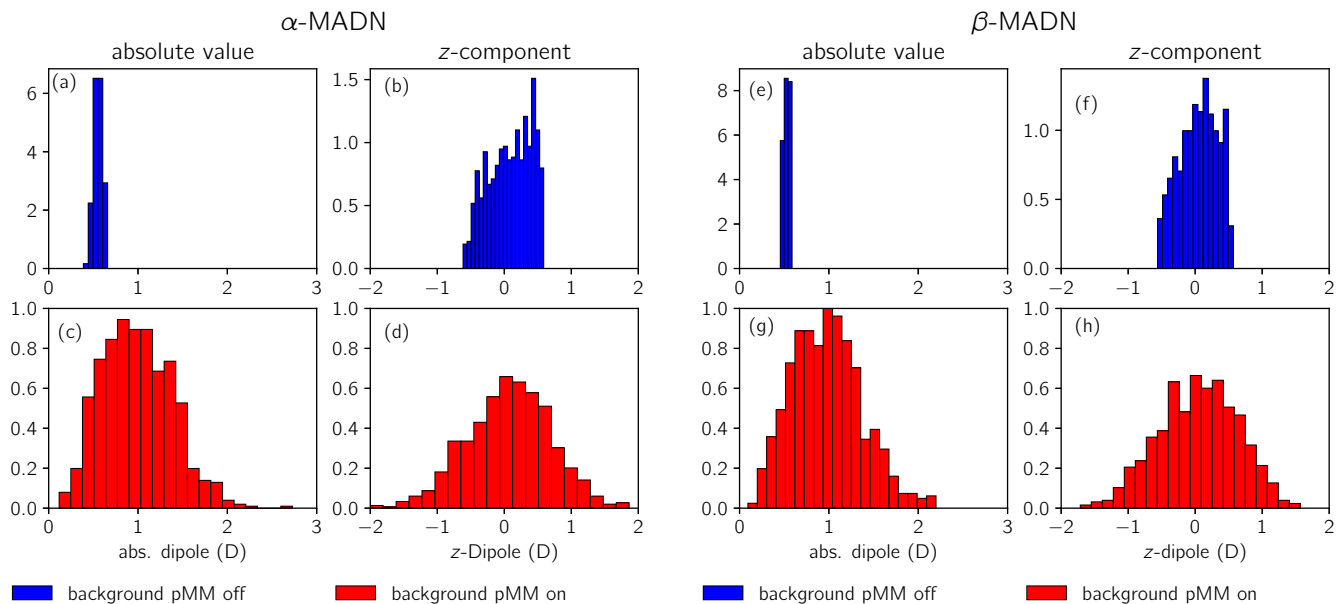


FIG. S3: Distributions of the absolute value and z -component of molecular dipoles for both α -MADN and β -MADN inside the amorphous films. Without the pre-polarization of the periodic neutral background (background pMM off, (a) and (b) for α -MADN and (e) and (f) for β -MADN) both distributions are quite narrow. When background pMM is on ((c) and (d) for α -MADN, (g) and (h) for β -MADN) induction effects tend to smear out the dipoles' orientation and strength. See text for further discussion.

and in the bulk-like region of the β -MADN film, respectively. One can clearly see a slow decrease with size of the embedding region, indicating in particular for the surface molecule that even at a cutoff of 20 nm no converged result is obtained. This highlights the need for a more efficient treatment of the long-range interactions taking an infinite periodic embedding into account. VOTCA-XTP currently only supports this in a *subtractive scheme*, in which the molecule in the QM region is also represented by the MM model and a purely classical energy correction $E_{\text{MM}}^{(n)} - E_{\text{MM}}^{(\text{qp})}$ is added to the GW vacuum energies. In the parametrization of the classical representation, we approximate the molecule's state after excitation of the GW HOMO by its cation. To validate this choice, we first repeat the analysis of the cutoff range dependence in this GW /cMM scheme as given by the red lines in Fig. S2 to the GW /pMM one. The comparison reveals deviations smaller than 0.02 eV. Based on this good agreement, we then use this parametrization and embed the classically represented QM molecule in a periodically repeated background. In this GW /pMM setup, the effects of the infinitely extended background is evaluated via an Ewald technique.²¹ The results for both the surface and the bulk molecule are shown as data points for $r_c = \infty$ in Fig. S2. For the surface molecule, the periodically embedded HOMO energy results 0.07 eV lower than in the GW /cMM calculation with the largest cutoff considered. In the bulk, the difference is with 0.03 eV slightly smaller. In the following, we focus on further details of how the GW /pMM method is used to obtain the results presented in the main text.

B. Electrostatic properties of the thin film and background polarization

When the thin film morphology is taken directly from the deposition simulation, the electrostatic properties of the constituent molecules are determined by their static multipole moments, here computed from classical atomic point charge distributions. At the same time, the film's electrostatic properties are directly given by the sum of these non-interacting multipoles. For both systems, we observe an accumulation of the dipole moment parallel to the surface normal (z -direction) of in total 65.6 D (α -MADN) and 35.7 D (β -MADN). Figure S3(a) and (e) show the distributions of the absolute dipole moment for α - and β -MADN, respectively. Both are narrow and centered around the single molecule values of 0.59 D and 0.56 D. From the distribution of the dipole moment's z -component (i.e., its component parallel to the surface normal) in Fig. S3(b) and (f) one can clearly see that there are more molecular dipoles aligned in positive z -direction which gives rise to the observed overall dipole moment of the thin film.

Due to interactions among the molecular dipole moments as obtain from single-molecule data, it can be assumed that a more realistic description of the thin films' electrostatic properties should include mutual polarization effects.

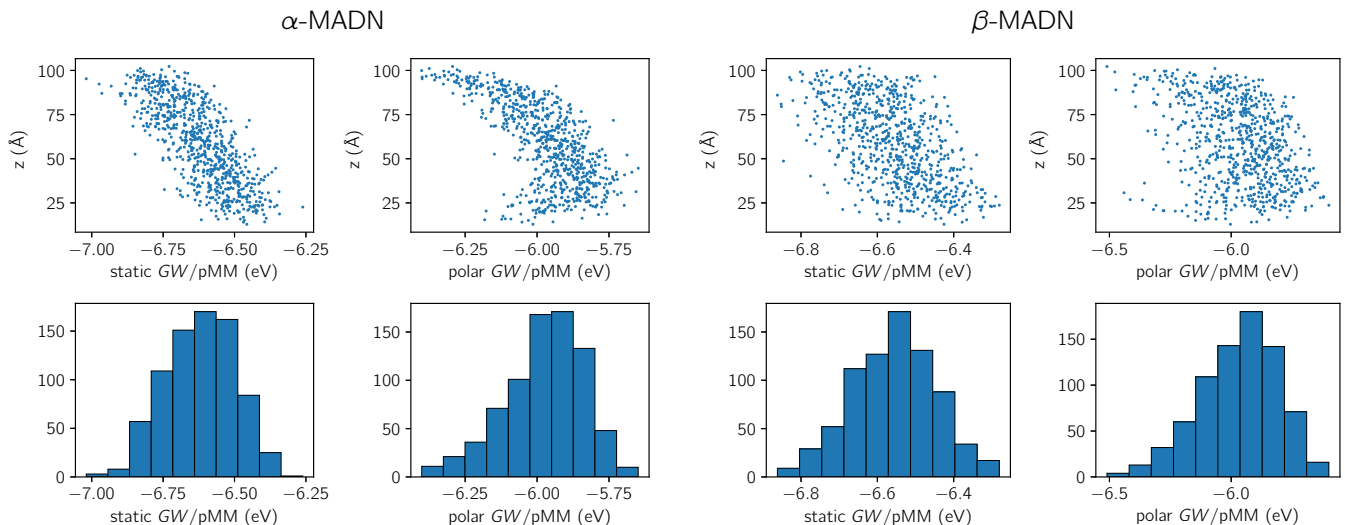


FIG. S4: Energies of the HOMO as obtained by static and polar GW/pMM simulations for the thin films of α -MADN and β -MADN, respectively. Upper panels show the energies resolved according to the z -component of the individual molecule's center-of-mass, while the lower panels show the total energy distribution (or the total density-of-states) in the respective films.

In our framework, we therefore first treat the total polarization of the film within the pMM approach described above (note that no quantum region is introduced and the whole system is charge neutral). After application of this background pMM, induced moments primarily lead to a broadening of the distribution of the absolute molecular dipole moments, as can be seen in Fig. S3(c) and (g). Similar observations can be made for the respective z -component distributions in Fig. S3(d) and (h). Induction reduces the total accumulated dipole moment in the film by 3.5 D (α -MADN) and 2.8 D (β -MADN).

C. Excitation energy distributions

In spite of the small effective reduction of the accumulated thin film dipole moment, the distributions in Fig. S3 suggest that the electrostatic potential inside the film and its surfaces shows strong local variations. These manifest themselves directly in a substantial amount of disorder in the calculated excitation energies within the GW/pMM approach. In the *static* GW/pMM case, the excitation is introduced into the pre-polarized neutral periodic background but no further polarization response due to the presence of an extra charge is included. For the *polar* GW/pMM calculations, an additional aperiodic region is defined by a cutoff distance of $r_c = 3$ nm around the QM molecule. In this region, the polarization response to the charged excitation is determined according to Eq. 10 and its energy correction evaluated as in Eq. 11. Layer-averaged profiles of the obtained HOMO energies are shown in Fig. 1 of the main text. For completeness, we show in Fig. S4 the individual HOMO energies as a function of the z -coordinate of the molecule's center-of-mass, as well as their total distributions.

S5. ESTIMATION OF THE ELECTRON INELASTIC MEAN FREE PATH

As mentioned in the main text, we consider the inelastic mean free path (IMFP) of the electrons, λ_{in} , as an upper limit to the electron attenuation length. In the following we focus on estimates of the IMFP within the modeling framework established in this work.

The IMFP represents the mean distance between successive inelastic collisions experienced by an electron in a material. Its energy dependence can be estimated with the help of the Energy Loss Function (ELF),

$$\text{Im} \left[\frac{-1}{\epsilon(q, \omega)} \right] = \frac{\epsilon_2(q, \omega)}{\epsilon_1(q, \omega)^2 + \epsilon_2(q, \omega)^2}, \quad (12)$$

where $\epsilon_1(q, \omega)$ and $\epsilon_2(q, \omega)$ are the real and the imaginary parts of the dielectric function, respectively. The ELF represents the probability of a material to absorb energy $\hbar\omega$ and momentum $\hbar q$ from an energetic incoming particle,

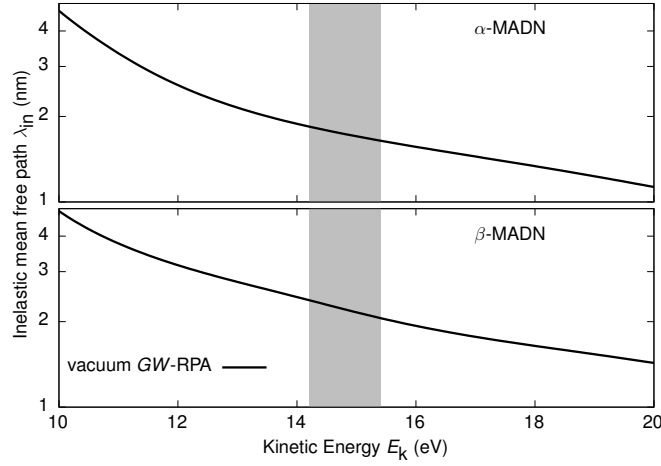


FIG. S5: Kinetic energy dependence of the IMFP in (a) α -MADN and (b) β -MADN as obtained based on RPA with vacuum *GW* quasiparticle energies. The gray shaded area indicates the range of interest (14.2 eV - 15.4 eV).

such as a photon or an electron with kinetic energy E_k . The IMFP is related to the ELF (in a.u.) via

$$\lambda_{\text{in}}^{-1}(E_k) = \frac{1}{\pi E_k} \int_{\omega_{\text{min}}}^{\omega_{\text{max}}} \int_{q_-}^{q_+} \frac{1}{q} \text{Im} \left[\frac{-1}{\epsilon(q, \omega)} \right] dq d\omega, \quad (13)$$

where $\omega_{\text{min}} = E_{\text{gap}}$, $\omega_{\text{max}} = (E_k + E_{\text{gap}})/2$, $q_{\pm} = \sqrt{2E_k} \pm \sqrt{2(E_k - \omega)}$.

The first step is to compute the ELF. To this end we firstly evaluate $\epsilon_2(0, \omega)$ according to the non-interacting electron-hole picture in the Random-Phase Approximation (RPA) as

$$\epsilon_2(0, \omega) = 16 \pi^2 \sum_{v,c} |\langle \phi_v^{\text{QP}} | \hat{D} | \phi_c^{\text{QP}} \rangle|^2 \delta(\omega - \epsilon_c + \epsilon_v), \quad (14)$$

where the sum runs over the occupied (v) and unoccupied states (c) and \hat{D} is the dipole moment operator. The real part of the full dielectric function is then obtained using the Kramers-Kronig relation. From this one can straightforwardly obtain the ELF in the optical limit ($q \rightarrow 0$) using Eq. 12.

Extending the ELF into the finite- q region is achieved using a model in which the dielectric response of the system is given by a summation of non-interacting component oscillators. In the RPA, valence electrons in the material are approximated by a non-interacting homogeneous gas where the plasmon energy is expanded to the second order in q

$$\text{DL}(q, \omega, \omega_p) = \frac{\gamma \omega_p \omega}{(\omega^2 - (\omega_p + \omega(q))^2)^2 + (\gamma \omega)^2}, \quad (15)$$

where $\omega(q) = E_{\text{gap}} + \alpha q^2$ and γ is the damping coefficient. The above optical Drude-Lorentz (DL) ELF in the form of Eq. 15 has a singularity at the plasma frequency ω_p .

To adapt this approach from a non-interacting to an interacting medium, we consider the optical ELF as composed of DL-ELF terms with closely spaced plasma frequencies ω_i such that

$$\text{Im} \left[\frac{-1}{\epsilon(0, \omega)} \right] = \sum_i A_i \text{DL}(0, \omega, \omega_p = \omega_i). \quad (16)$$

Once we have found the amplitude parameters A_i via a fitting procedure to our calculated ELF, we can build a momentum-dependent ELF according to

$$\text{Im} \left[\frac{-1}{\epsilon(q, \omega)} \right] = \sum_i A_i \text{DL}(q, \omega, \omega_p = \omega_i) \quad (17)$$

with the extension to finite q as in Eq. 15. Entering Eq. 17 into Eq. 13, we perform the integration over q and ω numerically to obtain $\lambda_{\text{in}}(E_k)$. For He-I UPS (photon energy 21.2 eV) and with ϵ_i in the range of -7.0 to -5.8 eV (see Fig. 1 of the main text), the kinetic energy of interest is approximately 14.2-15.4 eV. Figure S5 shows the kinetic

energy dependence of the IMFP as obtained with vacuum quasiparticle energies. For $E_k = 15.0$ eV we obtain IMFPs of 1.69 nm for α -MADN and 2.14 nm for β -MADN.

These values should be considered as upper limits to the real IMFP, and hence also the EAL, due to the neglect of, e.g., changes in the full quasiparticle spectrum due to morphology effects, intermolecular excitations in the RPA, or excitonic effects. Furthermore, elastic processes can additionally reduce the electrons' mean free path and hence the attenuation length. Explicit inclusion of these additional scattering mechanisms in our estimates is beyond the scope of this work.

From coverage-dependent studies of the He-I (21.2 eV) UPS spectrum of MADN on Au, we find (1) that the Au-contribution to the spectrum has not yet decreased significantly for a coverage of 0.6 nm (α -MADN), (2) that this contribution has decreased to about 10% for a coverage of 1.2 nm (β -MADN), and (3) that this contribution has almost vanished for a coverage above 1.6 nm (α -MADN).²² Given the uncertainties in obtaining the attenuation length from theory, detailed above, and based on these experimental observations, we regard the value of the attenuation of 1 nm, adopted in the main text for both isomers, as a fair estimate.

-
- * Electronic address: g.tirimbo@tue.nl
 † Corresponding author; Electronic address: b.baumeier@tue.nl
- ¹ T. Neumann, D. Danilov, C. Lennartz, and W. Wenzel, *J Comput Chem* **34**, 2716 (2013).
 - ² P. Friederich, R. Coehoorn, and W. Wenzel, *Chem. Mater.* **29**, 9528 (2017).
 - ³ P. Friederich, V. Rodin, F. von Wrochem, and W. Wenzel, *ACS Appl. Mater. Interfaces* **10**, 1881 (2018).
 - ⁴ B. H. Besler, K. M. Merz, and P. A. Kollman, *J. Comput. Chem.* **11**, 431 (1990).
 - ⁵ J. Wehner, L. Brombacher, J. Brown, C. Junghans, O. Çaylak, Y. Khalak, P. Madhikar, G. Tirimbò, and B. Baumeier, *J Chem Theory Comput* **14**, 6253 (2018).
 - ⁶ G. Onida, L. Reining, and A. Rubio, *Rev Mod Phys* **74**, 601 (2002).
 - ⁷ L. J. Sham and T. M. Rice, *Phys Rev* **144**, 708 (1966).
 - ⁸ L. Hedin and S. Lundqvist, in *Solid State Physics*, edited by F. Seitz, D. Turnbull, and H. Ehrenreich (Academic Press, 1970), vol. 23, pp. 1–181.
 - ⁹ L. Hedin, *Phys Rev* **139**, A796 (1965).
 - ¹⁰ G. Strinati, *Riv. Nuovo Cimento* 1978-1999 **11**, 1 (1988).
 - ¹¹ M. S. Hybertsen and S. G. Louie, *Phys Rev Lett* **55**, 1418 (1985).
 - ¹² W. G. Aulbur, L. Jönsson, and J. W. Wilkins, in *Solid State Physics*, edited by H. Ehrenreich and F. Spaepen (Academic Press, 2000), vol. 54, pp. 1–218.
 - ¹³ M. Rohlfing, *Int J Quantum Chem* **80**, 807 (2000).
 - ¹⁴ M. Rohlfing, P. Krüger, and J. Pollmann, *Phys Rev B* **52**, 1905 (1995).
 - ¹⁵ M. Valiev, E. J. Bylaska, N. Govind, K. Kowalski, T. P. Straatsma, H. J. J. Van Dam, D. Wang, J. Nieplocha, E. Apra, T. L. Windus, et al., *Comput. Phys. Commun.* **181**, 1477 (2010).
 - ¹⁶ M. A. L. Marques, M. J. T. Oliveira, and T. Burnus, *Comput. Phys. Commun.* **183**, 2272 (2012).
 - ¹⁷ R. A. Kendall, T. H. Dunning, and R. J. Harrison, *J Chem Phys* **96**, 6796 (1992).
 - ¹⁸ F. Weigend, A. Köhn, and C. Hättig, *J. Chem. Phys.* **116**, 3175 (2002).
 - ¹⁹ A. Stone, *The Theory of Intermolecular Forces, 2nd Edition* (Oxford University Press, Oxford, 2013), 2nd ed., ISBN 978-0-19-967239-4.
 - ²⁰ L. Cao and U. Ryde, *Front Chem* **6**, 89 (2018).
 - ²¹ C. Poelking, M. Tietze, C. Elschner, S. Olthof, D. Hertel, B. Baumeier, F. Würthner, K. Meerholz, K. Leo, and D. Andrienko, *Nat Mater* **14**, 434 (2015).
 - ²² C.H.L. Weijtens, unpublished.